

A Rapid Graphene Sensor Platform for the Detection of Viral Proteins in Low Volume Samples

Ffion Walters,* Gregory Burwell, Jacob John Mitchell, Muhammad Munem Ali, Ehsaneh Daghigh Ahmadi, A. Bernardus Mostert, Cerys Anne Jenkins, Sergiy Rozhko, Olga Kazakova, and Owen J. Guy*

Infectious disease outbreaks remain an ever-prevalent global issue. The associated demand for rapid diagnostics and onsite testing will play an increasing and critical role in disease surveillance, prevention of the spread of infection, as well as timely commencement of treatment. Reported here is a graphene–gold nanoparticle hybrid sensor platform technology that is demonstrated for the real-time detection of viral proteins utilizing low volume samples (5 μL). Hepatitis C virus (HCV) is still an endemic problem worldwide and is used as an exemplar system here to demonstrate the capability of the platform viral detection sensor technology. Hepatitis C virus core antigen (HCVcAg) is a promising marker for point-of-care (POC) diagnostic testing for active HCV infection, with the potential to provide a one-stop diagnosis and trigger for the commencement of treatment. Real-time electrical resistance measurements are performed using various concentrations of HCVcAg with linear concentration dependence of resistance on HCVcAg concentration over the range of 100–750 pg mL^{-1} .

(SARS-CoV-2) pandemic from 2019. One specific issue that has been highlighted by the pandemic is the need for methods to achieve rapid, accurate diagnostics for infectious diseases, not just for coronaviruses, but for other major diseases as well. Rapid diagnostics and onsite testing will therefore play a critical role in facilitating early intervention and treatment^[2] of diseases. Large-scale testing and rapid onsite diagnostic decisions are crucial for surveillance monitoring of disease outbreaks and infection spread. In future, this data will enable swift decision-making and management to help prevent the spread of epidemic and pandemic infectious disease outbreaks.^[1,3,4] In this work, we use the chronic hepatitis C virus (HCV) as a model infectious disease to demonstrate a viral detection platform sensor. HCV is still

endemic in populations around the world and is a major cause of liver cirrhosis and hepatocellular carcinoma, affecting around 71 million people worldwide.^[5] HCV deaths exceed annual deaths due to HIV, malaria, and tuberculosis.^[6] Consequently, the World Health Organization (WHO) aims to eliminate HCV by 2030,^[7,8] with a strategy to target an increase in HCV


1. Introduction

Infectious disease outbreaks remain an ever-prevalent global issue, with increasing global travel and trade increasing the risk of rapid disease spread to pandemic levels.^[1] This is exemplified by the severe acute respiratory syndrome coronavirus 2

F. Walters, J. J. Mitchell, M. M. Ali, E. Daghigh Ahmadi, O. J. Guy
Centre for NanoHealth, School of Engineering and Applied Sciences
Swansea University
Swansea SA2 8PP, UK
E-mail: f.a.walters@swansea.ac.uk; o.j.guy@swansea.ac.uk

G. Burwell
Department of Physics, School of Biosciences, Geography and Physics
Swansea University
Swansea SA2 8PP, UK

J. J. Mitchell
SPTS Technologies Ltd, R&D and Product department
Ringland Way, Newport NP18 2TA, UK

 The ORCID identification number(s) for the author(s) of this article can be found under <https://doi.org/10.1002/anbr.202100140>.

© 2022 The Authors. Advanced NanoBiomed Research published by Wiley-VCH GmbH. This is an open access article under the terms of the Creative Commons Attribution License, which permits use, distribution and reproduction in any medium, provided the original work is properly cited.

DOI: 10.1002/anbr.202100140

A. B. Mostert, O. J. Guy
Department of Chemistry, School of Engineering and Applied Sciences
Swansea University
Swansea SA2 8PP, UK

C. A. Jenkins
Swansea University Medical School
Swansea University
Swansea SA2 8PP, UK

S. Rozhko, O. Kazakova
National Physical Laboratory
Quantum Metrology Institute
Teddington, Middlesex TW11 0LW, UK

diagnosis and treatment. This strategy urgently requires simplified diagnostic tests for use in low-resource settings, as well as for difficult-to-reach populations in high-income countries.^[6,9,10]

The treatment of HCV has developed significantly since the introduction of direct-acting antiviral agents (DAAs), curing the vast majority of chronic HCV cases.^[5,11] HCV diagnosis usually requires two steps, serologic testing confirming exposure, such as anti-HCV antibody tests, followed by nucleic acid testing (NAT) to confirm active infection.^[12] HCV RNA (ribonucleic acid) tests, although highly accurate, can be relatively time-intensive, require expensive equipment and highly trained operators, providing a barrier for reengagement between healthcare providers with difficult-to-reach populations and low-resource settings.

Point-of-care (POC) tests are sought as the method to deliver a diagnosis as they are affordable, easy-to-use, portable, require small volume samples and fewer reagents, enabling rapid detection, and potentially allowing the immediate commencement of treatment.^[13–15] Currently, the majority of POC HCV tests are limited in that they can only detect previous exposure (HCV antibodies) and not active infection (HCV RNA or HCV core antigen); detection of the latter is required to commence treatment.^[6,16]

Therefore, realizing POC tests that can rapidly sanction initiation of treatment requires confirmation of the virological infection, i.e., HCVcAg detection.^[17] HCVcAg has been demonstrated to be highly stable across different individuals and is highly correlated with HCV RNA viral load.^[12] As such, assessment of HCVcAg levels alone may be sufficient to confirm an active HCV infection, allowing for a DAA prescription and bypassing the requirement for an HCV RNA test.^[12,11] Therefore, HCVcAg maybe a simple and affordable marker/tool for POC test development, facilitating and accelerating the successful elimination of HCV^[18] in difficult-to-reach populations and/or low-resource settings.

Currently, fingerstick sampling techniques have been implemented in various viral tests to facilitate more rapid diagnosis.^[6] These tests are currently in development for HCV POC diagnostics.^[19] It would therefore be advantageous to develop a POC platform for infectious diseases, e.g., HCV, that utilizes small volume samples and therefore enables the use of fingerstick sampling. This could facilitate single-engagement testing for patients, avoiding multiple reengagement requirements for low-resource or difficult-to-reach populations.^[20] Rapid tests, yielding results in real time and using small volume samples, will therefore be a key enabler to achieving the WHO's goal of HCV elimination, with high sensitivity an essential attribute required for detection of HCVcAg and replacement of NAT tests in certain settings.

Graphene, a material which has been investigated extensively for sensing applications,^[21–26] is potentially an ideal material for highly sensitive tests required for one-off testing and subsequent treatment initiation regimes. Graphene has a very high surface-to-volume ratio and is ultrasensitive to its chemical environment, with the capability for single gas molecule detection.^[27–29] With suitable surface modification strategies, graphene real-time sensors offer a highly sensitive platform for rapid POC diagnostics for viral markers including for HCV. Graphene field-effect transistors (GFETs) and

resistor-based sensors can be utilized for sensing applications as they are highly sensitive, have a simple device configuration, are low cost, can be miniaturized, with the feasibility for real-time detection of biomarkers^[30] demonstrated in the literature for the detection of various analytes including viral proteins.^[13,31,32]

Sensitive, specific detection of HCVcAg requires surface modification of graphene to elicit a specific response to the analyte. This surface modification has two components: 1) a mechanism for recognition or detection of an analyte, and 2) a system that can anchor the recognition/detection system to the graphene surface.

There are several strategies available for anchoring molecules to graphene surfaces, including covalent^[33–36] and noncovalent methods,^[37–39] the latter of which takes advantage of π - π stacking. The use of anchoring groups attached noncovalently via π - π stacking is well established for graphene having been demonstrated with molecules including 1,5-diaminonaphthalene,^[23,40–42] oligonucleotides,^[13,43,44] and 1-pyrenebutanoic acid succinimidyl ester (PBASE)^[26,45] for sensor development. Pyrene has also been widely utilized for this purpose.^[27,46–48] Adsorption of the pyrene onto the basal planes of graphene allows robust noncovalent end attachment of polyethylene glycol (PEG) chains to graphitic surfaces,^[49] and specific to graphene, pyrene groups stack via π - π overlap to form a self-assembled monolayer.^[25,50] If the PEG is then capped with a thiol moiety, it can be utilized for further functionalization. The strength of the π - π stacking between the graphene surface and the aromatic molecules of the functionalization layer means that the surface stacking is robust enough to be maintained after rinsing or other solution processing^[40,51,52] and therefore facilitates simple drop-cast functionalization techniques. It should be noted that the electronic properties of graphene can be manipulated through modification of the surface, via both covalent and noncovalently methods—detectable as a change in the graphene resistance after anchoring of groups to the graphene surface.

With regard to the recognition/detection system for HCVcAg, gold nanoparticles (AuNPs) are an excellent candidate. AuNPs have been used to enhance signals in biosensors, leading to the creation of graphene–AuNP hybrids.^[13,53–55] AuNPs can provide a stable and robust immobilization platform for biomolecules^[56] and well-known functionalization strategies exist,^[57] particularly in relation to Au-thiol chemistry. The AuNPs facilitate an interface with a large surface area for receptor binding, due in part to increased deflection angle of the bio-receptors which potentially reduces steric hindrance in comparison to planar surfaces.^[13,58] AuNPs have therefore been used to increase sensitivity and the linear dynamic range of graphene sensors.^[59,60]

In this work, we present a strategy for detecting HCVcAg that has broader implications for rapid detection of viruses in clinical settings. To our knowledge, this is the first reported use of a graphene resistor-based biosensor to detect HCVcAg in real-time. We demonstrate graphene resistor devices that have been functionalized with AuNPs that can specifically respond to HCVcAg. However, to our knowledge, our functionalization approach is novel in its use of PEG–SH linkers, in conjunction with the overall biofunctionalization strategy; using ex situ decoration of prefunctionalized AuNPs is also previously unreported. A clear differential to background responses related to sensor exposure to the surrounding media is reported as well as the use of

isotherm analysis to confirm the preferential attachment of an antigen to binding sites on functionalized AuNPs in a graphene sensor system. Sensitive graphene sensors, of microscale dimensions, are demonstrated to detect HCVcAg via AuNPs while simultaneously allowing for the use of small volume samples facilitating the potential for fingerstick sample collection for POC testing of HCV. This extremely adaptable platform technology can deliver highly sensitive viral protein detection, opening avenues toward population screening and hard-to-reach population testing.

2. Results and Discussion

2.1. Characterization of Graphene

Graphene was characterized using Raman spectroscopy (Figure 1a), both before (pristine chemical vapor deposition [CVD] graphene) and as part of the final device architecture (following channel etching and aluminum oxide [Al₂O₃] passivation; Figure 1b).

Raman spectroscopy is widely used on graphene as a characterization technique and typical analyses focus on the D, G, and 2D bands, located around 1300, 1600, and 2600 cm⁻¹, respectively. Raman spectra can be used to verify single-layer graphene from the intensity ratio of the 2D to G band (I_{2D}/I_G), with pristine graphene yielding a ratio of ≈ 2 .^[13,61–63] Any damage to the graphene carbon lattice structure, resulting from the device fabrication process, will lead to an increase in the D peak,^[64] and as

such the quality of the devices can be assessed. Figure 1a shows two representative Raman spectra, with corresponding Raman maps displayed in Figure S1, Supporting Information. Peak analysis from the unmodified graphene material reveals an I_{2D}/I_G ratio of ≈ 2.5 , consistent with pristine, monolayer graphene. The graphene channel in the final device architecture reveals a smaller I_{2D}/I_G ratio of ≈ 1.6 which may be due to defects or impurities related to the device fabrication steps. Defects in the graphene structure provide nucleation sites for the molecular vapor deposition (MVD) growth in the Al₂O₃ passivation process. This provides a “healing effect” and is known to reduce surface organic contaminants, such as photoresist, from CVD graphene.^[65–67] A device independence check was carried out on a chip, consisting of two separate devices (Figure 1c), to confirm the devices were discrete. Real-time data can be found in Figure 1d.

2.2. Functionalized Graphene

2.2.1. Characterization of the Functionalization Layer

The pristine graphene was first functionalized with pyrene–PEG–thiol (Pyr–PEG–SH) via a drop-cast method, followed by drop-casting of the AuNPs, prefunctionalized with anti-HCVcAg antibody, onto the Pyr–PEG–SH functionalized graphene. Attachment of the functionalized AuNP to the Pyr–PEG–SH-modified graphene surface is via a linking reaction between gold and the thiol moiety (see Figure 2a for a depiction of the functionalization). To confirm the presence of the

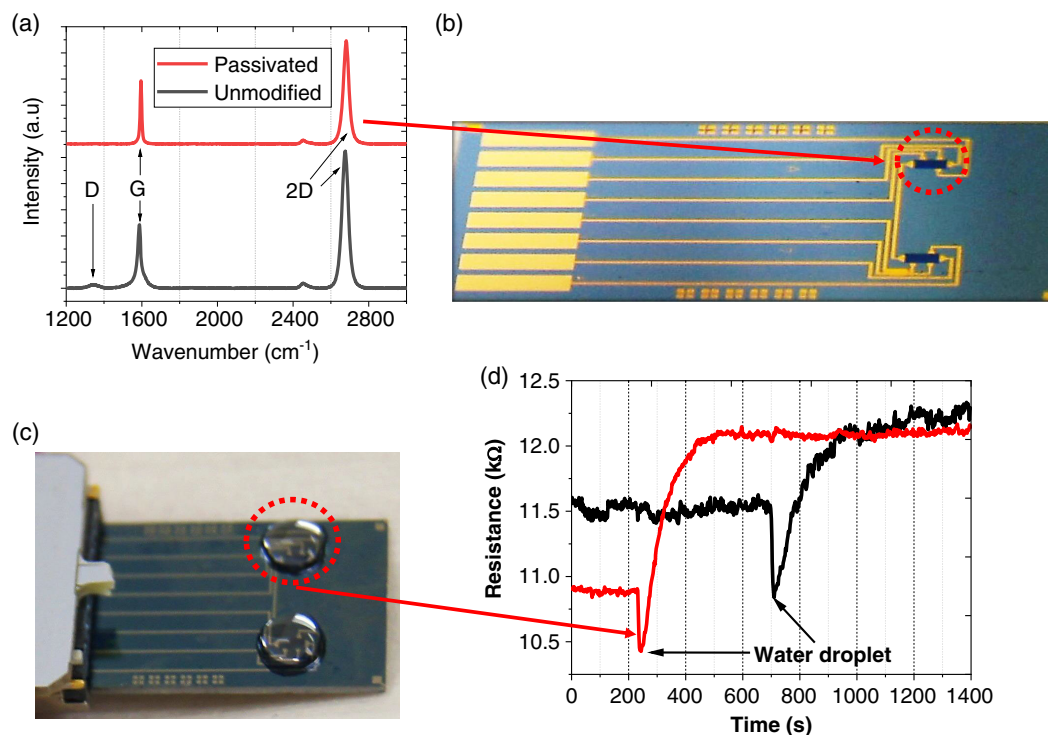


Figure 1. a) Raman spectra normalized and averaged from map scans of CVD graphene before channel etching and passivation (gray) and after channel etching and passivation (red). b) Fabricated, passivated “DipChip” graphene device. c) 5 μ L droplets pipetted on to the active area of the graphene device. d) Real-time resistance measurements of 2 \times graphene resistor devices on a single chip, after 5 μ L of deionized (DI) water was applied to each resistor device. The devices show independent signals while being measured simultaneously.

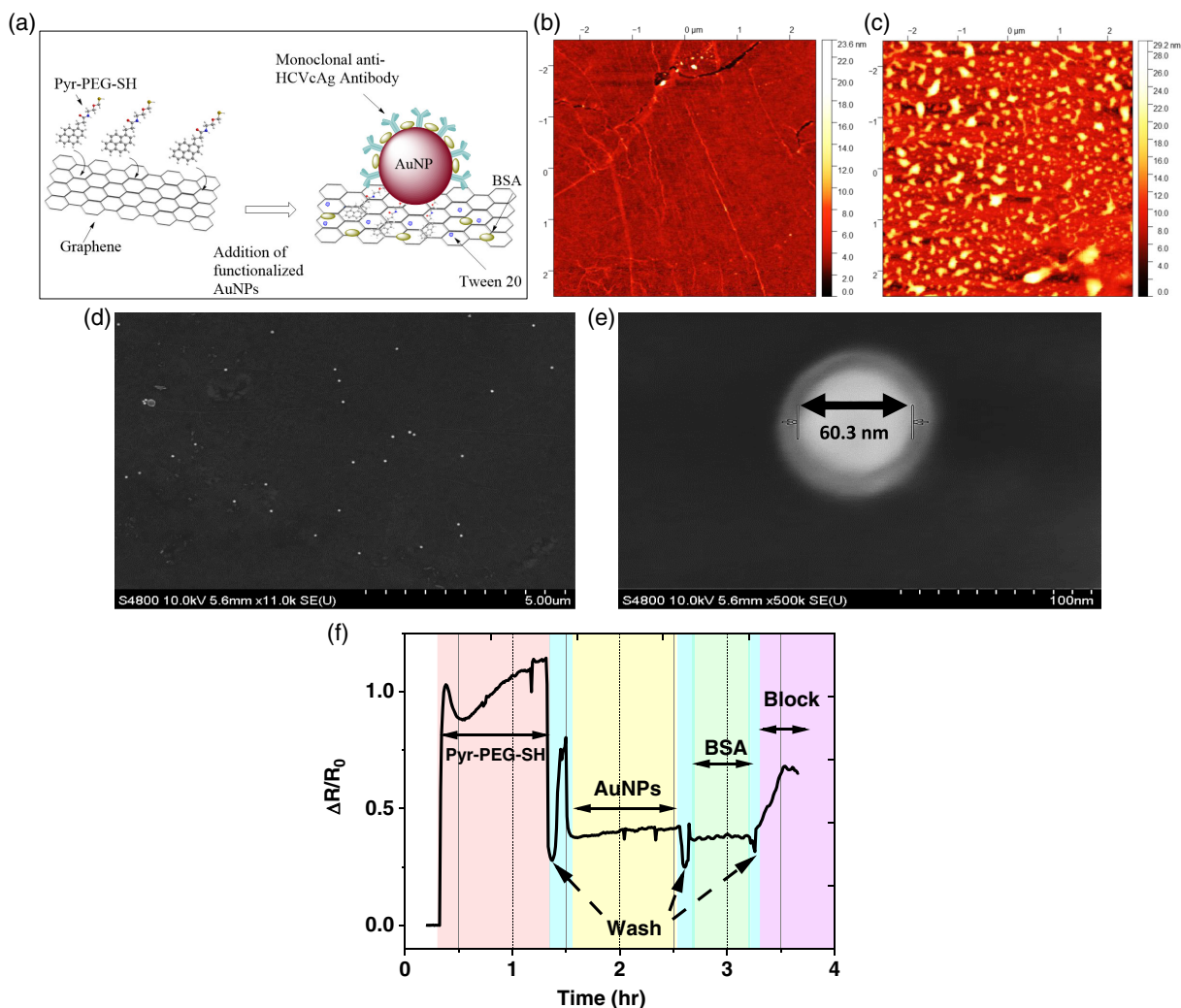


Figure 2. a) Schematic of the functionalization method. b) AFM image of CVD graphene before functionalization. c) AFM image of CVD graphene after functionalization with Pyr-PEG-SH and DI water wash. d) SEM images of AuNPs on the graphene device surface. e) Higher magnification SEM image of a single AuNP, confirming the size of the particle to be 60 nm. f) Real-time resistance measurements of the graphene functionalization process in solution, where $\Delta R = R_{\text{Device}} - R_0$, and R_0 is the intrinsic device resistance. Wash = Droplet removed via pipette, 10 μL of DI water added and mixed via pipette, the DI water droplet was removed, with the process repeated three more times.

Pyr-PEG-SH linker on the graphene surface, atomic force microscopy (AFM) images were obtained of both pristine CVD graphene (Figure 2b) and the modified CVD graphene after a DI water wash (Figure 2c). The figures clearly indicate that the surface of the graphene has been modified, with RMS roughness (S_q) of 745 pm and 3.51 nm for the pristine and modified CVD, respectively. The attachment of the AuNPs was also investigated using scanning electron microscopy (SEM) (Figure 2d,e). The gold particles are clearly detectable on the surface and the particle size consistent with the supplier's data sheet for the AuNPs.

2.2.2. Real-Time Resistance Measurements of Surface Functionalization

Surface modification of the graphene was also monitored in real-time utilizing electrical measurements (Figure 2f), using time

dependence of the relative resistance change, $\Delta R/R_0$. Repeat data can be found in Figure S2, Supporting Information. An increase in resistance of the graphene device was observed when Pyr-PEG-SH (in DI water) was added to the surface and incubated at room temperature (RT) for 1 h. In our tests, the devices were washed without interrupting the electrical measurements: first by removing the droplet of functionalization solution by pipette, and then 10 μL DI water was added to the device and removed by pipette, with the process repeated three times. Each functionalization step leads to a change in resistance (Figure 2f), in relation to the previous step, indicating the response of graphene to the different functionalization solutions.

The graphene doping (and resistance) depends on the type of the interactions with electron donor versus electron-withdrawing systems.^[68] For example, graphene on a SiO_2 substrate is typically p-doped under ambient conditions.^[69] For molecular

systems, when π - π stacked molecules are electron donors, i.e., electrons transfer to the graphene, this results in n-type doping of the graphene, whereas p-type doping will originate from molecules acting as electron acceptors.^[51,70] In our case, pyrene, which has neither electron-donating or electron-withdrawing groups, has been shown to have little to no doping effect on graphene.^[71] In contrast, PEG-SH has been shown to cause n-doping.^[39] Therefore, the change in the resistance on addition of the Pyr-PEG-SH solution (Figure 2f) is likely due to the n-doping effect of the PEG-SH linker (in DI water), where the n-doping of the p-doped graphene on SiO₂ would shift the graphene toward its charge neutrality point, leading to an increase in resistance.

Pyr-PEG-SH also serves as a linker connecting graphene to the functionalized AuNPs. A decrease in $\Delta R/R_0$ is observed on addition of the AuNP solution, relative to the Pyr-PEG-SH solution in the previous functionalization step; this could suggest a p-doping effect related to this step.

One issue to consider in the design of sensing devices is non-specific binding (NSB). NSB is undesirable in sensing applications as it reduces the sensitivity of the sensors. It is therefore essential to minimize NSB in general but especially when utilizing highly sensitive materials such as graphene and/or dealing with very low analyte concentrations. Due to the sensitive nature of graphene and the complexity of functionalization, requiring multiple stages/chemical reactions/linking groups, etc., several blocking steps may be required to quench each reaction, bind out unreacted moieties, and block unbound surfaces. It might be advantageous to use multiple blockers to perform different/complementary roles within the sensor development. To that end, two separate blocking steps were utilized here. Bovine serum albumin (BSA) was used to block any sites on the AuNPs not already taken up by the antibody as well as providing some initial blocking of the graphene surface. A second blocking solution was then used to block the remainder of the graphene surface, containing both BSA and tween 20. Tween 20 has been used to block various 2D materials^[26,72] and has been shown to provide optimized blocking capabilities when used in conjunction with other blocking agents such as BSA.^[73] It contains an aliphatic chain that can attach to the hydrophobic graphene

surface via noncovalent interactions, and aliphatic ester chains that can help to prevent nonspecific binding.^[46] The effect of these blockers on the electrical resistance of the graphene device is also shown in Figure 2f, where further changes in resistance are observed on addition of both the BSA and blocking solutions relative to the previous functionalization step.

2.3. Detection Experiment

2.3.1. Real-Time Electrical Detection of HCVcAg

Real-time HCVcAg sensing was performed using the functionalized graphene resistor devices, measuring the resistance changes in response to sequential increases of HCVcAg concentration (Figure 3). Typical sample volumes in the literature for similar real-time graphene sensors vary between 10 and 40 μL ^[13,23,25,31]; this work aims to evaluate even smaller volume samples, i.e., 5 μL . Each measurement involved application of a 5 μL droplet of HCVcAg solution (diluted in 1 \times phosphate-buffered saline (PBS) (pH 7.4) to a given concentration) onto the channel window of the functionalized graphene-AuNP hybrid device, and incubation for 20 min at RT. The initial droplet was then removed via pipette and a droplet with higher HCVcAg concentration was applied to the channel window, while the resistance of the device was continuously monitored. This process was repeated for all HCVcAg concentrations increasing from 0 to 750 pg mL^{-1} .

Figure 3a shows the normalized real-time resistance responses of an example device, as a function of HCVcAg concentration (additional results can be found in Figure S3, Supporting Information). Analysis of reproducibility can be found in Figures S6 and S7, Supporting Information. The addition of higher HCVcAg concentrations leads to an increase in the resistance, suggesting a charge transfer of electrons to the graphene,^[13] i.e., n-type doping.

The sensor shows a limit of detection (LoD) (positive change in $\Delta R/R_0$) of 100 pg mL^{-1} , based on a signal that exceeds 3 \times the background signal (average $\Delta R/R_0$ plotted against HCVcAg concentration can be found in Figure S4, Supporting Information). One potential advantage of using sensors for POC applications is

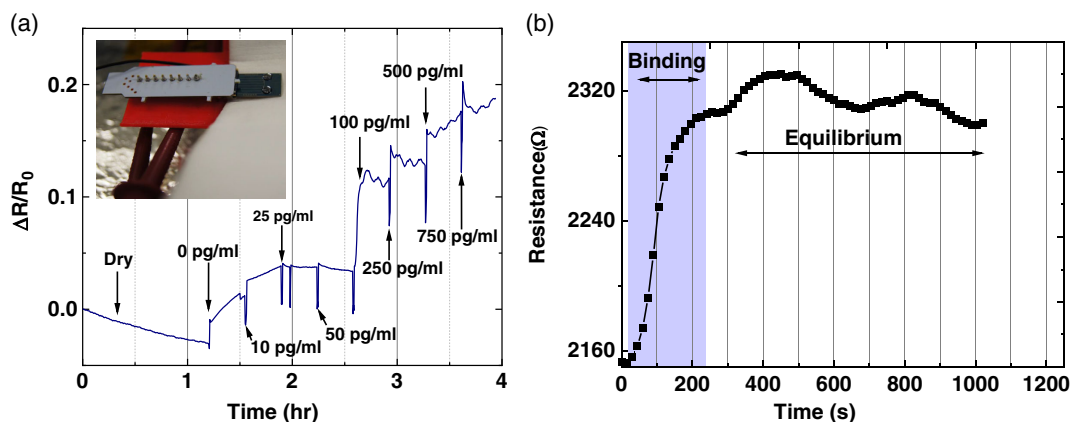


Figure 3. a) Graphene device resistance response to the time-dependent application of various HCVcAg concentrations in pg mL^{-1} . Inset graphene device chip attached to an electrical connector, with two 5 μL samples (one applied on each graphene resistor). b) Response time of the sensor on the addition of 100 pg mL^{-1} of HCVcAg.

the speed at which a result can be obtained. For example, Figure 3b shows the sensor's reaction to the addition of 100 pg mL^{-1} HCVcAg, with the signal reaching equilibrium at $\approx 225 \text{ s}$ ($< 4 \text{ min}$). However, there is potential for this to be improved further with optimization of the system.

The real-time resistance measurements (Figure 3a) were taken using bottom-contact graphene resistor devices, where the metal contacts are situated beneath the graphene layer. HCVcAg sensing was also carried out on top-contact graphene resistor devices, where the metal contacts are fabricated on top of the graphene, for comparison (sensing data can be found in Figure S5, Supporting Information). No difference in sensor performance was observed due to contact type.

One suggested detection mechanism for graphene–AuNP hybrid sensors is attributed to conductivity changes produced when target analytes bind to the immobilized receptors which may lead to a carrier concentration change in graphene, due to the effective electronic transfer between the graphene and AuNPs.^[56,57,74] The resistance was recorded as a function of time; additions of HCVcAg further increase the resistances observed, from that at the functionalization stage, suggesting a charge transfer of electrons to the graphene.^[13] However, further studies are required to conclusively determine the critical contributing factors to electrical resistance changes.

2.3.2. Specificity Investigation

The graphene sensor response to increasing concentration of HCVcAg is encouraging. However, the specificity of the sensor needs to be confirmed. Specificity has been investigated, using a nonspecific protein (BSA), introduced at increasing concentrations between 0 and 750 pg mL^{-1} , in a procedure similar to that for HCVcAg, described above. Real-time results (Figure 4a and Figure S8, Supporting Information) show that the BSA does demonstrate some changes in $\Delta R/R_0$ but, overall, does not produce the same trend in $\Delta R/R_0$ as observed for HCVcAg. Indeed, unlike the HCVcAg results, concentration dependence (indicated by $\Delta R/R_0$ in a positive direction) was not observed across the testing range for the BSA negative control protein, even when a much higher concentration (500 ng mL^{-1}) of BSA was introduced (Figure 4b). This result suggests that specific antigen–antibody binding is responsible for the concentration-dependent positive changes in $\Delta R/R_0$ for HCVcAg detection.

A further control experiment was carried out, utilizing bare (unfunctionalized) AuNPs attached to the graphene via Pyr–PEG–SH (see Supplementary Information for details), to investigate whether physisorption of proteins to the surface of the AuNP (e.g., if particle surfaces were not fully blocked) could contribute to/mask the specific signal generated, i.e., the concentration-dependent $\Delta R/R_0$ seen for the HCVcAg sensing. The real-time resistance was monitored for increasing BSA concentrations between 0 and 750 pg mL^{-1} (Figure 4c), using the same methodology as detailed above (further repeats and analysis can be found in Figures S8 and S10, Supporting Information). Again, no $\Delta R/R_0$ trend in a positive direction, was observed for the non-functionalized AuNP control, adding further to the suggestion that the positive HCVcAg sensing is a true result and not due to the physisorption of proteins.

Another aspect of the testing regime to be considered is the response of the sensor to the testing buffer solution. PBS is used in the initial test as it is representative of physiological conditions^[75] and as such is used in many sensor development works. As real-time measurements were realized and therefore samples of increasing concentration were measured sequentially, any potential signal changes generated due to the use of sequential PBS additions should therefore also be controlled for. The real-time resistance response of bare (intrinsic) graphene devices to multiple sequential PBS ($1 \times \text{PBS}$, pH 7.4) additions was investigated. Some changes were observed, with $\Delta R/R_0$ increasing for the first two PBS additions (Figure 4d); further repeats and analysis can be found in Figures S8 and S9, Supporting Information). These changes potentially originate from n-doping of graphene by PBS caused by the screening of negative charges at the surface (on Si/SiO₂ substrates),^[25] as well as charge stabilization.^[76] Further PBS application reverses the trend and leads to the decrease of $\Delta R/R_0$; one possible explanation for this could be salt deposition. Increasing exposure to PBS has been shown to affect the conductance of graphene.^[60] No sequential change of $\Delta R/R_0$ in the positive direction was observed across the seven PBS additions, suggesting that detection of HCVcAg (Figure 3, S3 and S5, Supporting Information), shown by concentration dependence ($\Delta R/R_0$ in a positive direction), is a true positive result and is not due to buffer effects or the sequential nature of the testing regime.

The effect of PBS only on an example functionalized device was also studied using Hall bar resistance measurements and compared to measurements taken on the dry device (Figure 4e). Real-time Hall measurements consisted of a dry measurement followed by the addition of $4 \text{ }\mu\text{L}$ of $1 \times \text{PBS}$ (pH7.4) placed on the channel window of the functionalized graphene–AuNP hybrid device and incubated for $\approx 15 \text{ min}$ at RT. Changes in carrier concentration of the graphene were observed when comparing the dry functionalized device ($p = 1.8 \text{ p} \times 10^{12} \text{ cm}^{-2}$), and the same device exposed to the $1 \times \text{PBS}$ (pH7.4) solution ($p = 1.2 \text{ p} \times 10^{12} \text{ cm}^{-2}$). This again shows that the effect of the buffer on the sensor should be accounted for as it can affect the signal generated. Therefore, buffer effects on the sensor before and during measurements are an important consideration in biosensor design and signal analysis and interpretation.

2.3.3. Analysis

The time-averaged response of the real-time data was extracted using a Matlab script. The local minima displayed in the real-time data were used as reference points corresponding to times where a droplet had been added to the surface. Average values were extracted for iterative measurements of $1 \times \text{PBS}$ (pH 7.4) on a bare graphene device. The average values are plotted against the iteration number in Figure 5a.

Time-averaged data for responses to HCVcAg and BSA (negative control protein) are shown in Figure 5b. Here, the PBS response was subtracted from the time-averaged data points and renormalized for comparison. This clearly shows a positive $\Delta R/R_0$ response to the HCVcAg with increasing concentration, whereas the BSA response is relatively flat at high concentrations, after an initial negative response at low

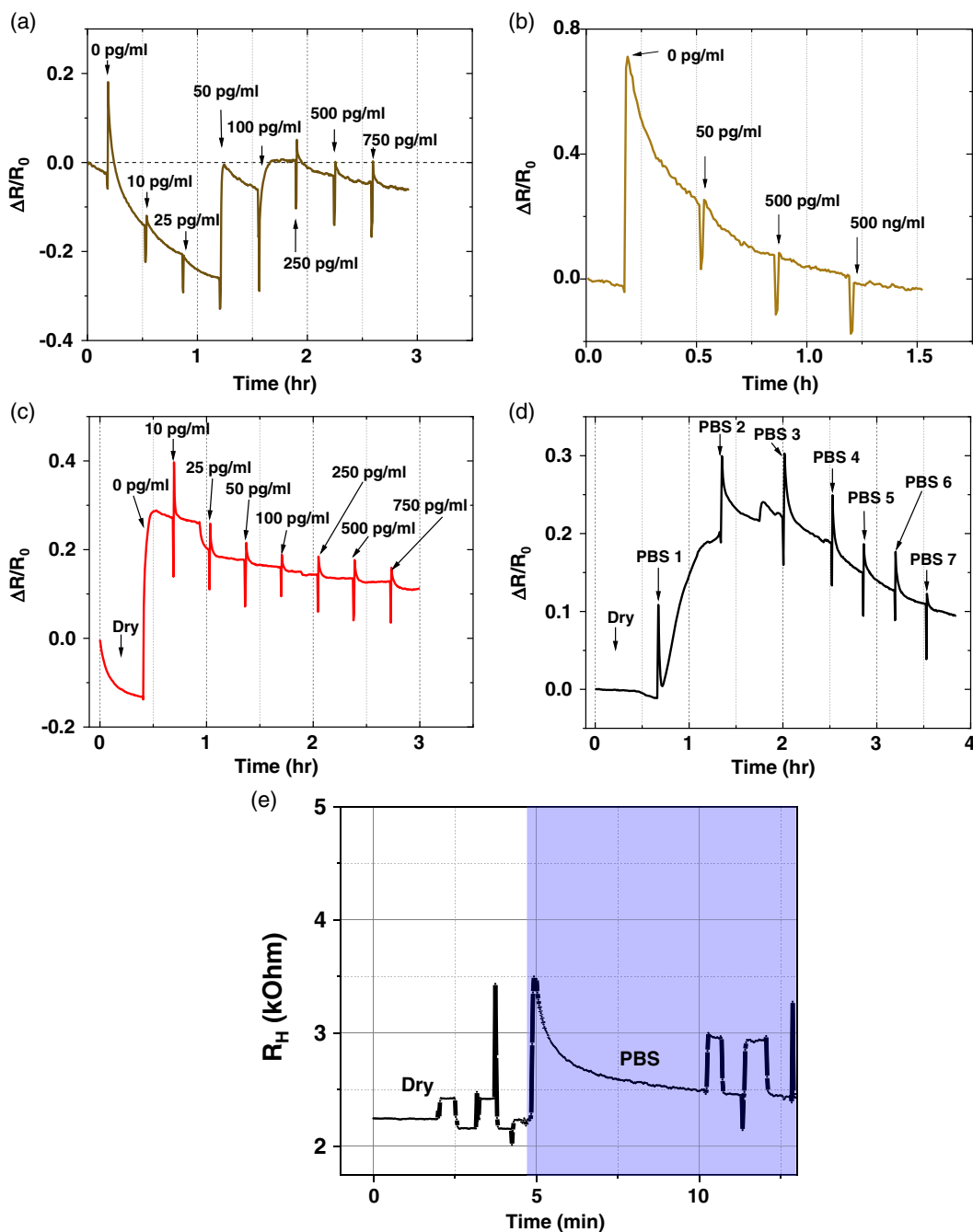


Figure 4. Functionalized graphene–AuNP hybrid device (with anti-HCVcAg functionalized AuNPs) resistance response to the time-dependent application of BSA concentrations: a) 0, 10, 25, 50, 100, 250, 500, and 750 pg mL^{-1} . b) 50 pg mL^{-1} , 500 pg mL^{-1} and 500 ng mL^{-1} . c) Unfunctionalized AuNP (bare AuNPs) graphene–AuNP hybrid device resistance response to the time-dependent application of BSA concentrations 0, 10, 25, 50, 100, 250, 500, and 750 pg mL^{-1} . d) Unfunctionalized Graphene device (bare graphene) resistance response to the time-dependent application of multiple sequential $1 \times$ PBS (pH7.4) droplets. e) Time dependence of the Hall resistance for a functionalized graphene device in the dry state (unshaded) and in PBS (shaded in blue).

concentrations, which could be due to graphene charging behavior.^[76] Taking the $\Delta R/R_0$ signal (of the BSA negative control) as the baseline response, the LoD of the positive signal, taken as $3 \times$ this signal baseline, is consistent with the LoD of 100 pg mL^{-1} calculated in Section 2.3.1.

The PBS-corrected average $\Delta R/R_0$ values were then plotted as a function of concentration to yield an adsorption isotherm (Figure 5c). Given that adsorption processes are at work, investigation of the behavior may yield some additional insight, e.g., such data can describe the heterogeneity of a surface.^[77]

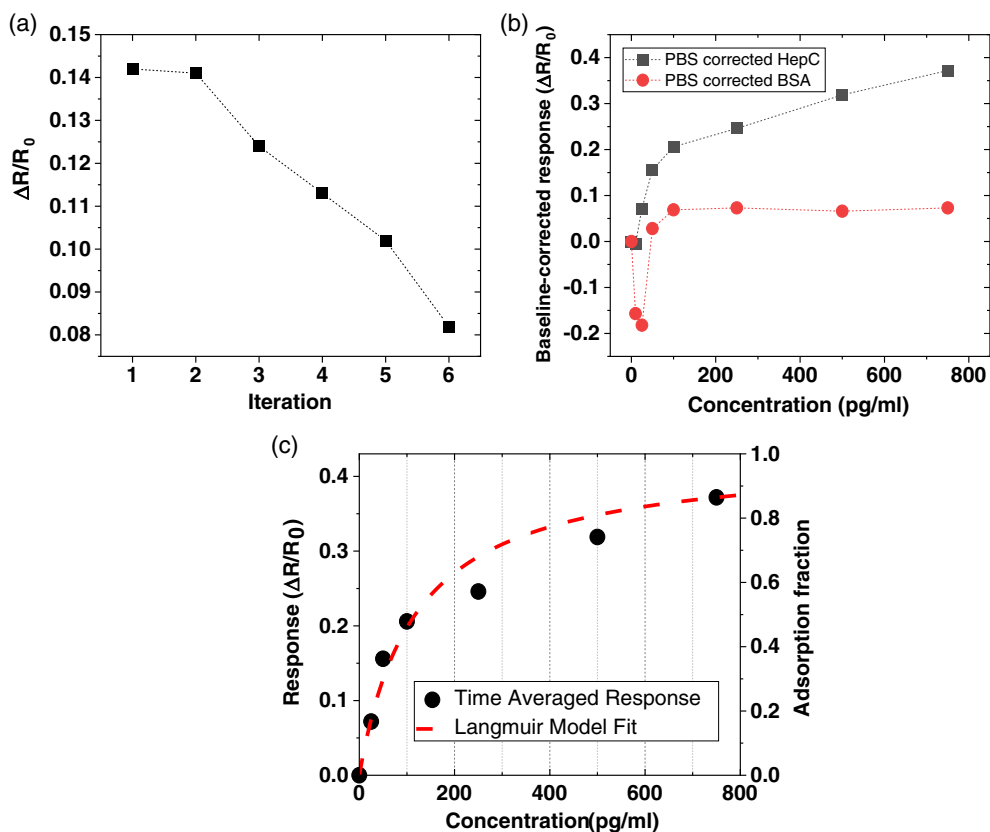


Figure 5. a) The time-averaged response of an unfunctionalized graphene device to iterative applications of the same PBS solution. b) The PBS-corrected time-averaged response of functionalized devices to HCVcAg (black curve) and BSA (red curve). c) Fit of the background-corrected HCVcAg response on a functionalized device to a Freundlich-type isotherm.

A versatile isotherm model that is often used to describe adsorption out of aqueous solutions (such as our system) is the Langmuir–Freundlich isotherm or Sip’s equation^[77,78]

$$\frac{n}{N} = \frac{(KC)^\alpha}{1 + (KC)^\alpha} \quad (1)$$

where n is the amount adsorbed (mol g^{-1}), N is the adsorption capacity (mol g^{-1}), K is the equilibrium or affinity constant (mL pg^{-1}) for the adsorption process, C is the aqueous phase concentration (pg mL^{-1}), and α is the index of heterogeneity. The last variable has a range of 0–1, with 1 yielding the Langmuir adsorption isotherm, indicating a material with only one kind of homogenous site, whereas values less than 1 indicate increasing heterogeneity. The utility of this simple model is the limited number of fitting parameters that one needs to describe the system. The data from Figure 5c were transformed from $\Delta R/R_0$ to an adsorption fraction (right y -axis) after modeling to a Langmuir isotherm (i.e., $\alpha = 1$), as shown in Figure 5c (see Supplementary information for full procedure). A similar approach was attempted for a generalized Langmuir–Freundlich equation, but no stable least squares result could be determined for α within the 0–1 range, indicating that the Langmuir isotherm provides the most accurate representation of the experimental data. The modeling indicated an equilibrium

constant of $(8.5 \pm 3.8) \times 10^{-3} \text{ mL pg}^{-1}$. The use of a Langmuir isotherm in detecting viral particles has precedence, where the authors used a similar principle to detect the particles as demonstrated in this work.^[79] The Langmuir model result, suggest that one has monolayer adsorption of particles on only one kind of site, which would be an indication of the specificity for the HCVcAg by the modified AuNPs on the surface, with little to no competition from other sites (e.g., the rest of the graphene surface), as would be indicative of a lower value for α . However, the scatter of the data at high concentrations away from the model line is notable, and as such it may indicate an interaction of the HCVcAg with the graphene surface that is much weaker than the specific interaction with the AuNP-bound sites. Such an interaction would likely be nonspecific in nature, due to the absence of any specific binding sites on the graphene surface.

Overall, these results suggest that the binding of the HCVcAg to the functionalized sites on the AuNPs has an initial strong absorption coefficient to sterically available sites on the AuNP (i.e., anti-HCVcAg antibody-binding sites). Deviations from the proposed binding model may be due to the nonspecific, weak binding of HCVcAg to the basal plane of bare graphene. This suggests that blocking strategies for the graphene basal plane to improve selectivity would not interfere with the high sensitivity given by the preferential binding of HCVcAg to the AuNP antibody binding sites. This is in contrast to the

nonspecific response of BSA. The BSA response is more consistent with a linear response from physisorption at high concentrations. Crucially, our specific (antigen–antibody) and nonspecific (physiosorbed) responses are opposite in direction. This type of trend is consistent with previous reports in the literature.^[32,80,81]

3. Conclusions

A real-time graphene–AuNP hybrid sensor for the detection of viral proteins has been demonstrated using a small sample volume (5 μL). HCV was used as an exemplar system to demonstrate the platform sensor technology. HCVcAg has been shown to correlate to HCV RNA viral load and therefore is a promising marker toward HCV POC diagnostics. The sensor showed good sensitivity to HCVcAg at $\geq 100 \text{ pg mL}^{-1}$ with relatively low AuNP densities, demonstrating the potential of the graphene–AuNP sensor design when fully optimized. A slight nonspecific response to BSA was observed, which we attribute to physisorption at the graphene surface. Full optimization of the sensor is required, but this proof-of-concept work is an initial step toward a real-time platform technology for sensitive detection of viral protein markers while also utilizing small volume samples. This could open opportunities for sensing using finger-stick blood samples which could be especially beneficial in resource-limited settings or for difficult-to-reach populations. The platform can be applied easily to other infectious disease markers, including markers for hepatitis B virus (HBV) and SARS-CoV-2 for COVID-19 POC diagnostics, human immunodeficiency virus (HIV), and many more.

4. Experimental Section

Materials: Wafer substrate: Si with dry thermal SiO_2 supplied by Si-Mat GmbH Graphene CVD monolayer transfer service supplied by Hexagon Fab Ltd. Photolithography supplies for metal lift-off: Microchem LOR 3 A positive photoresist; Microposit S1805 G2 Positive resist; Microposit MF-CD-26 developer all supplied from DOW Electronics Materials. Photolithography supplies for patterning: AZ 5214 E photoresist, AZ 726 Developer, AZ 100 Remover, Technistrip Micro D350 all supplied from Microchemicals GmbH. Trimethylaluminum (TMA) and DI H_2O ALD precursors supplied by Pegasus Chemicals Ltd. $1 \times \text{PBS}$ containing 0.01 M phosphate, 0.0027 M KCl, and 0.137 M NaCl, pH 7.4, Hepatitis C Core Antigen and anti-HC Core antigen antibody, bovine serum albumin (BSA) and all other reagents (analytical grade) supplied by Sigma Aldrich.

Raman Spectroscopy: An InVia Raman microspectrometer (Renishaw, UK) was used to collect Raman spectroscopic data with a spectrometer equipped with a $100 \times$ NPlan microscope objective (Leica, USA). Spectral data were acquired using a 532 nm laser with a 2400 L mm^{-1} spectral grating. Representative spectra are shown in Figure 1a and indicate the presence of monolayer graphene. Raman spectra of the entire surface were taken in a number of scans (i.e., a Raman map), the average of which was taken to yield a representative Raman spectrum. Raman maps can be found in Figure S1, Supporting Information.

AFM: AFM was performed using a JPK NanoWizard II system. Bruker Sharp Nitride Lever (SNL-10) probes were used in tapping mode, with a nominal tip radius of 2 nm and fundamental frequency of 65 KHz. Representative $5 \times 5 \mu\text{m}$ scans were taken across the surface, and data were processed by row alignment and removal of a polynomial background.

Graphene Device Fabrication: The graphene devices used in this work were fabricated using CVD graphene onto SiO_2/Si wafers and were manufactured according to the methods outlined in our previous work.^[13,65] Graphene devices were fabricated on a 300 nm thermal oxide SiO_2/Si 100 mm wafer (p-type, 1–10 Ohm resistivity, orientation $< 100^\circ$). The metal contacts were deposited using physical vapor deposition, 30 nm Cr and 200 nm Pd (Kurt J Lesker PVD75). CVD monolayer graphene was then transferred onto the SiO_2 substrate with patterned metal contacts. The graphene Hall bar channels were then patterned using photolithography (AZ 5214 E photoresist) and subsequently etched using O_2 plasma. The devices were then passivated with a 50 nm Al_2O_3 (using an SPTS Technologies MVD 300).^[65] A window on the Al_2O_3 passivation layer was then patterned using photolithography (AZ 5214E photoresist) and subsequent wet chemical etching of Al_2O_3 using TMAH 2.38%. Further details of device fabrication can be found in the supplementary information along with a schematic (Figure S11, Supporting Information).

Pyr–PEG–SH Functionalization: 10% solution of Pyr–PEG–SH (2000 Da) diluted in DI water was drop-cast onto the graphene devices ($10 \mu\text{L}$) and incubated at RT for 1 h. Devices were subsequently washed in situ with $3 \times 10 \mu\text{L}$ DI water.

Gold Nanoparticle Functionalization: Gold nanoparticles (60 nm) were functionalized with monoclonal anti HCVcAg antibodies. A $16 \mu\text{L}$ of 0.1 mg mL^{-1} antibody solution was added to 1 mL of AuNPs (OD1) and left to conjugate for 1 h at RT under mixing.

Graphene–AuNP Hybrid Manufacture: Anti-Hep C functionalized AuNPs were drop-cast onto the Pyr–PEG–SH functionalized graphene devices and incubated at RT for 1 h. Devices were washed in situ with $3 \times 10 \mu\text{L}$ DI water.

Blocker Attachment: BSA blocker (1%) diluted in DI water, drop-cast onto the Pyr–PEG–SH/AuNP functionalized graphene devices, and incubated for 30 min at RT. Devices were washed in situ with $3 \times 10 \mu\text{L}$ DI water.

Secondary Blocking Step: Blocking buffer consisting of $1 \times \text{PBS}$ (pH 7.4) + 1% BSA + 0.5% Tween 20 was drop-cast on the Pyr–PEG–SH/AuNP/BSA functionalized devices and incubated at RT for 30 min. Devices were washed in situ with $3 \times 10 \mu\text{L}$ DI water.

Electrical Measurements: Graphene “DipChips” with two CVD graphene resistor channels on a SiO_2/Si substrate were used for sensitive real-time 2-point resistance measurements. A “Sensor-Connect” connector (supplied by Biovici Ltd.) was used to provide electrical connections between the graphene channels and the measurement instruments. A fixed-voltage measurement regime was used throughout (40 mV). Measurements were carried out under ambient conditions (temperature 20°C , normal atmospheric pressure). A device independence check was carried out on a chip, consisting of two separate devices, to confirm the devices were discrete. Real-time data can be found in Figure 1d.

$\Delta R/R_0$ used throughout where $\Delta R = R_{\text{Device}} - R_0$, and R_0 is the intrinsic resistance of the functionalized device in dry state at time, $t = 0$.

Hall Resistance Measurements: Hall resistances were measured using the 4-terminal lock-in technique. The Hall voltage was measured when the magnetic field of both polarities (two polarities were used to eliminate the voltage offset contribution) were applied perpendicular to the graphene surface. The measurements were performed using the following parameters

Bias current, I bias = 100 nA

Frequency, $f = 11 \text{ Hz}$

Magnetic field density, $\pm 0.78 \text{ T}$

Magnetic field was applied when the resistance was close to the equilibrium state.

Charge carrier concentration, p , is calculated from the measured Hall resistance, R_H , by the formula

$$p = \frac{B}{RH * e} \quad (2)$$

where e is the elementary electron charge; B is the magnetic field density.

Statistical Analysis: Preprocessing: A custom MATLAB script was used to extract average normalized resistance ($\Delta R/R_0$) from real-time data.

Local minima in the time series were used to identify the points at which droplets were cast onto the graphene sensor surface. Devices with irregular responses were excluded from statistical analysis; these differences were attributed to variations in device manufacture.

Analysis of $n = 3$ representative devices gave monotonically increasing $\Delta R/R_0$, with increasing concentrations of HCVcAg had a mean $\Delta R/R_0$ of $+0.349$ and SD of 0.036 at a concentration of 750 pg mL^{-1} HCVcAg.

A total of $n = 2$ devices were used to analyze the effect of iterative exposure to PBS. A decreasing trend in $\Delta R/R_0$ was measured, with a mean $\Delta R/R_0 = -0.15$, $SD = 0.014$ after the seventh iterative addition of PBS.

A total of $n = 3$ devices were used to analyze the response of BSA on devices with unfunctionalized AuNPs. A decreasing trend in $\Delta R/R_0$ was measured, with a mean $\Delta R/R_0 = -0.13$, $SD = 0.015$ at a concentration of 750 pg mL^{-1} BSA.

Supporting Information

Supporting Information is available from the Wiley Online Library or from the author.

Acknowledgements

F.W. and G.B. contributed equally to this work. This research was funded by Innovate UK under Newton Fund—China—UK Research and Innovation Bridges Competition 2015 (Project ref.: 102877), Engineering and Physical sciences Research Council (Project ref.: EP/M006301/1), and Knowledge Economy Skills Scholarships (KESS). NPL acknowledges the support of the UK Government Department for Business, Energy and Industrial Strategy through the UK National Quantum Technologies Programme and EU Graphene Flagship under grant agreement GrapheneCore3 881603. The authors also acknowledge support from Avenues of Commercialisation of Nano & Micro Technologies (ACNM) Operation funded by the European Regional Development Fund via the Welsh Government. G.B. acknowledges funding from the Welsh Government Capacity Builder Accelerator Program through the European Regional Development Fund, Welsh European Funding Office, and Swansea University Strategic Initiative in Sustainable Advanced Materials. A.B.M. is a Sêr Cymru II fellow and the results incorporated in this work are supported by the Welsh Government through the European Union's Horizon 2020 research and innovation program under the Marie Skłodowska Curie grant agreement no. 663830. The authors also acknowledge the Application Specific Semiconductor Etch Technologies (ASSET) Project funded by the European Regional Development Fund via the Welsh Governments Smart Expertise Operation. J.J.M. acknowledges the support of the Knowledge Transfer Partnership Associate (Project number 011971) funded by Innovate UK and SPTS Technologies Ltd. Graphene device fabrication and passivation aided by the Centre for NanoHealth technical team. The authors would like to acknowledge Pegasus Chemicals Ltd. for the supply of chemicals used in MVD passivation. The authors would also like to acknowledge Biovici Ltd. for use of their "Sensor-Connect" technology for real-time resistance measurements. The authors would like to thank Mr. Thomas Chess for SEM imaging.

Conflict of Interest

The authors declare no conflict of interest.

Data Availability Statement

The data that support the findings of this study are available from the corresponding author upon reasonable request.

Keywords

chemiresistor, gold nanoparticles, graphene biosensor, hepatitis C virus core antigen (HCVcAg), hybrid, real-time

Received: October 28, 2021

Revised: March 4, 2022

Published online: March 22, 2022

- [1] C. H. Woo, S. Jang, G. Shin, G. Y. Jung, J. W. Lee, *Nat. Biomed. Eng.* **2020**, *4*, 1168.
- [2] X. Ding, K. Yin, Z. Li, R. V. Lalla, E. Ballesteros, M. M. Sfeir, C. Liu, *Nat. Commun.* **2020**, *11*, 4711.
- [3] T. Chaibun, J. Puenpa, T. Ngamdee, N. Boonapatcharoen, P. Athamanolap, A. P. O'Mullane, S. Vongpunsawad, Y. Poovorawan, S. Y. Lee, B. Lertanantawong, *Nat. Commun.* **2021**, *12*, 802.
- [4] W. Feng, A. M. Newbigging, C. Le, B. Pang, H. Peng, Y. Cao, J. Wu, G. Abbas, J. Song, D.-B. Wang, M. Cui, J. Tao, D. L. Tyrrell, X.-E. Zhang, H. Zhang, X. C. Le, *Anal. Chem.* **2020**, *92*, 10196.
- [5] H. Jiang, X.-X. Wang, B.-f. Luo, X. Cong, Q. Jin, H. Qin, H.-y. Zhang, X.-s. Kong, L. Wei, B. Feng, *Clin. Exp. Med.* **2019**, *19*, 299.
- [6] J. Grebely, B. Catlett, I. Jayasinghe, H. Valerio, B. Hajarizadeh, A. Verich, P. Cunningham, M. Martinello, S. Tillakeratne, D. Silk, G. J. Dore, T. L. Applegate, *J. Infect. Dis.* **2020**, *221*, 2043.
- [7] Z. Mohamed, J. Mbwambo, Y. Shimakawa, L. Poiteau, S. Chevaliez, J.-M. Pawlotsky, J. Rwegasha, S. Bhagani, S. D. Taylor-Robinson, J. Makani, M. R. Thursz, M. Lemoine, *J. Int. AIDS Soc.* **2017**, *20*, 21856.
- [8] E. Gupta, P. Agarwala, G. Kumar, R. Maiwall, S. K. Sarin, *Clin. Virol.* **2017**, *88*, 46.
- [9] B. N. Vetter, E. I. Reipold, S. Ongarello, R. Audu, F. A. Ige, M. Alkhazashvili, N. Chitadze, F. Vanroye, A. De Weggeheire, S. An, K. Fransen, *J. Infect. Dis.* **2020**, jiaa389.
- [10] World Health Organization, *Global Health Sector Strategy on Viral Hepatitis 2016–2021*, World Health Organization, Geneva **2016**.
- [11] B. Feng, R.-F. Yang, H.-J. Jiang, Y.-D. Xie, H.-Y. Zhang, Q. Jin, X. Cong, L. Wei, *Clin. Exp. Med.* **2020**, *20*, 131.
- [12] A. H. Talal, Y. Chen, M. Zeremski, R. Zavala, C. Sylvester, M. Kuhns, L. S. Brown, M. Markatou, G. A. Cloherty, *J. Subst. Abuse Treat.* **2017**, *78*, 37.
- [13] F. Walters, S. Rozhko, D. Buckley, E. D. Ahmadi, M. Ali, Z. Tehrani, J. Mitchell, G. Burwell, Y. Liu, O. Kazakova, O. J. Guy, *2D Mater.* **2020**, *7*, 024009.
- [14] E. T. S. G. da Silva, D. E. P. Souto, J. T. C. Barragan, J. de F. Giarola, A. C. M. de Moraes, L. T. Kubota, *ChemElectroChem* **2017**, *4*, 778.
- [15] B. Chakraborty, A. Das, N. Mandal, N. Samanta, N. Das, C. R. Chaudhuri, *Sci. Rep.* **2021**, *11*, 2962.
- [16] J. Grebely, T. L. Applegate, P. Cunningham, J. J. Feld, *Expert Rev. Mol. Diagn.* **2017**, *17*, 1109.
- [17] R. W. Peeling, D. I. Boeras, F. Marinucci, P. Easterbrook, *BMC Infect. Dis.* **2017**, *17*, 699.
- [18] F. M. J. Lamoury, A. Soker, D. Martinez, B. Hajarizadeh, E. B. Cunningham, P. Cunningham, P. Bruggmann, G. R. Foster, O. Dalgard, M. Backmund, B. Conway, G. Robaey, T. Swan, G. Cloherty, P. Marks, J. Grebely, G. J. Dore, T. L. Applegate, *J. Clin. Virol.* **2017**, *92*, 32.
- [19] I. Shahid, A. R. Alzahrani, S. S. Al-Ghamdi, I. M. Alanazi, S. Rehman, S. Hassan, *Diagnostics* **2021**, *11*, 1253.
- [20] S. Arca-Lafuente, P. Martínez-Román, I. Mate-Cano, R. Madrid, V. Briz, *J. Infect.* **2020**, *80*, 8.
- [21] J. Ping, R. Vishnubhotla, A. Vrudhula, A. T. C. Johnson, *ACS Nano* **2016**, *10*, 8700.

- [22] Z. Gao, H. Xia, J. Zauberman, M. Tomaiuolo, J. Ping, Q. Zhang, P. Ducos, H. Ye, S. Wang, X. Yang, F. Lubna, Z. Luo, L. Ren, A. T. Charlie Johnson, *Nano Lett.* **2018**, *18*, 3509.
- [23] J. Tu, Y. Gan, T. Liang, Q. Hu, Q. Wang, T. Ren, Q. Sun, H. Wan, P. Wang, *Front. Chem.* **2018**, *6*, 1.
- [24] Y. Li, Y. Zhu, C. Wang, M. He, Q. Lin, *Biosens. Bioelectron.* **2018**, *126*, 59.
- [25] D. Kwong Hong Tsang, T. J. Lieberthal, C. Watts, I. E. Dunlop, S. Ramadan, A. E. del Rio Hernandez, N. Klein, *Sci. Rep.* **2019**, *9*, 13946.
- [26] S. Ghosh, N. I. Khan, J. G. Tsavalas, E. Song, *Front. Bioeng. Biotechnol.* **2018**, *6*, 1.
- [27] S. Xu, J. Zhan, B. Man, S. Jiang, W. Yue, S. Gao, C. Guo, H. Liu, Z. Li, J. Wang, Y. Zhou, *Nat. Commun.* **2017**, *8*, 14902.
- [28] F. Schedin, A. K. Geim, S. V. Morozov, E. W. Hill, P. Blake, M. I. Katsnelson, K. S. Novoselov, *Nat. Mater.* **2007**, *6*, 652.
- [29] C. Melios, V. Panchal, K. Edmonds, A. Lartsev, R. Yakimova, O. Kazakova, *ACS Sens.* **2018**, *3*, 1666.
- [30] Q. He, S. Wu, Z. Yin, H. Zhang, *Chem. Sci.* **2012**, *3*, 1764.
- [31] S. J. Park, S. E. Seo, K. H. Kim, S. H. Lee, J. Kim, S. Ha, H. S. Song, S. H. Lee, O. S. Kwon, *Biosens. Bioelectron.* **2021**, *174*, 112804.
- [32] Z. Hao, Y. Zhu, X. Wang, P. G. Rotti, C. DiMarco, S. R. Tyler, X. Zhao, J. F. Engelhardt, J. Hone, Q. Lin, *ACS Appl. Mater. Interfaces* **2017**, *9*, 27504.
- [33] V. Mishyn, T. Rodrigues, Y. R. Leroux, P. Aspermaier, H. Happy, J. Bintingier, C. Kleber, R. Boukherroub, W. Knoll, S. Szunerits, *Nanoscale Horizons* **2021**, *6*, 819.
- [34] F. Rösicke, M. A. Gluba, T. Shaykhtudinov, G. Sun, C. Kratz, J. Rappich, K. Hinrichs, N. H. Nickel, *Chem. Commun. (Camb)* **2017**, *53*, 9308.
- [35] J. Greenwood, T. H. Phan, Y. Fujita, Z. Li, O. Ivasenko, W. Vanderlinden, H. Van Gorp, W. Frederickx, G. Lu, K. Tahara, Y. Tobe, H. Uji-i, S. F. L. Mertens, S. De Feyter, *ACS Nano* **2015**, *9*, 5520.
- [36] Z. Tehrani, G. Burwell, M. A. Mohd Azmi, A. Castaing, R. Rickman, J. Almarashi, P. Dunstan, A. Miran Beigi, S. H. Doak, O. J. Guy, *2D Mater.* **2014**, *1*, 025004.
- [37] S. Wang, M. Z. Hossain, K. Shinozuka, N. Shimizu, S. Kitada, T. Suzuki, R. Ichige, A. Kuwana, H. Kobayashi, *Biosens. Bioelectron.* **2020**, *165*, 112363.
- [38] R. Campos, J. Borme, J. R. Guerreiro, G. Machado, M. F. Cerqueira, D. Y. Petrovykh, P. Alpuim, *ACS Sensors* **2019**, *4*, 286.
- [39] N. M. Andoy, M. S. Filipiak, D. Vetter, Ó. Gutiérrez-Sanz, A. Tarasov, *Adv. Mater. Technol.* **2018**, *3*, 1800186.
- [40] F. Walters, M. M. Ali, G. Burwell, S. Rozhko, Z. Tehrani, E. D. Ahmadi, J. E. Evans, H. Y. Abbasi, R. Bigham, J. J. Mitchell, O. Kazakova, A. Devadoss, O. J. Guy, *Nanomaterials* **2020**, *10*, 1808.
- [41] D. H. Shin, J. S. Lee, J. Jun, J. H. An, S. G. Kim, K. H. Cho, J. Jang, *Sci. Rep.* **2015**, *5*, 12294.
- [42] J. H. An, S. J. Park, O. S. Kwon, J. Bae, J. Jang, *ACS Nano* **2013**, *7*, 10563.
- [43] L. Tang, Y. Wang, J. Li, *Chem. Soc. Rev.* **2015**, *44*, 6954.
- [44] A. Bonanni, A. Ambrosi, M. Pumera, *Chem. - A Eur. J.* **2012**, *18*, 1668.
- [45] G. Wu, X. Tang, M. Meyyappan, K. W. C. Lai, *Appl. Surf. Sci.* **2017**, *425*, 713.
- [46] W. Fu, L. Feng, G. Panaitov, D. Kireev, D. Mayer, A. Offenhäuser, H.-J. Krause, *Sci. Adv.* **2017**, *3*, 1.
- [47] X. V. Zhen, E. G. Swanson, J. T. Nelson, Y. Zhang, Q. Su, S. J. Koester, P. Bühlmann, *ACS Appl. Nano Mater.* **2018**, *1*, 2718.
- [48] C. Wang, X. Cui, Y. Li, H. Li, L. Huang, J. Bi, J. Luo, L. Q. Ma, W. Zhou, Y. Cao, B. Wang, F. Miao, *Sci. Rep.* **2016**, *6*, 21711.
- [49] A. Anne, M. A. Bahri, A. Chovin, C. Demaille, C. Taoffenua, *Phys. Chem. Chem. Phys.* **2014**, *16*, 4642.
- [50] S. R. Ahn, J. H. An, S. H. Lee, H. S. Song, J. Jang, T. H. Park, *Sci. Rep.* **2020**, *10*, 388.
- [51] Z. Zhang, H. Huang, X. Yang, L. Zang, *J. Phys. Chem. Lett.* **2011**, *2*, 2897.
- [52] B. J. Robinson, S. W. D. Bailey, L. J. O'Driscoll, D. Visontai, D. J. Welsh, A. B. Mostert, R. Mazzocco, C. Rabot, S. P. Jarvis, O. V. Kolosov, M. R. Bryce, C. Lambert, *ACS Nano* **2017**, *11*, 3404.
- [53] B. Nagar, M. Balsells, A. de la Escosura-Muñiz, P. Gomez-Romero, A. Merkoçi, *Biosens. Bioelectron.* **2019**, *129*, 238.
- [54] S. Gupta, R. Meek, *Sensors Actuators B Chem.* **2018**, *274*, 85.
- [55] I. Khalil, W. A. Yehye, N. M. Julkapli, S. Rahmati, A. A. I. Sina, W. J. Basirun, M. R. Johan, *Biosens. Bioelectron.* **2019**, *131*, 214.
- [56] S. Mao, G. Lu, K. Yu, Z. Bo, J. Chen, *Adv. Mater.* **2010**, *22*, 3521.
- [57] K. Chen, G. Lu, J. Chang, S. Mao, K. Yu, S. Cui, J. Chen, *Anal. Chem.* **2012**, *84*, 4057.
- [58] D. Kim, A. E. Herr, *Biomicrofluidics* **2013**, *7*, 041501.
- [59] R. Forsyth, A. Devadoss, O. Guy, *Diagnostics* **2017**, *7*, 45.
- [60] X. Dong, Y. Shi, W. Huang, P. Chen, L.-J. Li, *Adv. Mater.* **2010**, *22*, 1649.
- [61] L. M. Malard, M. A. Pimenta, G. Dresselhaus, M. S. Dresselhaus, *Phys. Rep.* **2009**, *473*, 51.
- [62] A. C. Ferrari, D. M. Basko, *Nat. Nanotechnol.* **2013**, *8*, 235.
- [63] Y. Bleu, F. Bourquard, A. Loir, V. Barnier, F. Garrelie, C. Donnet, *J. Raman Spectrosc.* **2019**, *50*, 1630.
- [64] L. G. Caçado, K. Takai, T. Enoki, M. Endo, Y. A. Kim, H. Mizusaki, *Appl. Phys. Lett.* **2006**, *88*, 163106.
- [65] M. M. Ali, J. J. Mitchell, G. Burwell, K. Rejnhard, C. A. Jenkins, E. D. Ahmadi, S. Sharma, O. J. Guy, *Nanomaterials* **2021**, *11*, 2121.
- [66] R. H. J. Vervuurt, W. M. M. E. Kessels, A. A. Bol, *Adv. Mater. Interfaces* **2017**, *4*, 1700232.
- [67] D. Van Lam, S.-M. Kim, Y. Cho, J.-H. Kim, H.-J. Lee, J.-M. Yang, S.-M. Lee, *Nanoscale* **2014**, *6*, 5639.
- [68] C. N. R. Rao, R. Voggu, *Mater. Today*, *13*, 34.
- [69] L. Banszerus, H. Janssen, M. Otto, A. Epping, T. Taniguchi, K. Watanabe, B. Beschoten, D. Neumaier, C. Stampfer, *2D Mater.* **2017**, *4*, 025030.
- [70] G. Wu, X. Tang, M. Meyyappan, K. W. C. Lai, in *2015 IEEE 15th Int. Conf. on Nanotechnology (IEEE-NANO)*, IEEE, Piscataway, NJ **2015**, pp. 1324–1327.
- [71] J. Lee, E. Hwang, E. Lee, S. Seo, H. Lee, *Chem. - A Eur. J.* **2012**, *18*, 5155.
- [72] N. Belkhamssa, C. I. L. Justino, P. S. M. Santos, S. Cardoso, I. Lopes, A. C. Duarte, T. Rocha-Santos, M. Ksibi, *Talanta* **2016**, *146*, 430.
- [73] M. V. Riquelme, H. Zhao, V. Srinivasaraghavan, A. Pruden, P. Vikesland, M. Agah, *Sens. Bio-Sensing Res.* **2016**, *8*, 47.
- [74] S. R. Russell, S. A. Claridge, *Anal. Bioanal. Chem.* **2016**, *408*, 2649.
- [75] A. Purwidyantri, T. Domingues, J. Borme, J. R. Guerreiro, A. Ipatov, C. M. Abreu, M. Martins, P. Alpuim, M. Prado, *Biosensors* **2021**, *11*, 24.
- [76] C. Reiner-Rozman, M. Larisika, C. Nowak, W. Knoll, *Biosens. Bioelectron.* **2015**, *70*, 21.
- [77] K. Y. Foo, B. H. Hameed, *Chem. Eng. J.* **2010**, *156*, 2.
- [78] G. P. Jeppu, T. P. Clement, *J. Contam. Hydrol.* **2012**, *129–130*, 46.
- [79] B. T. T. Nguyen, G. Koh, H. S. Lim, A. J. S. Chua, M. M. L. Ng, C.-S. Toh, *Anal. Chem.* **2009**, *81*, 7226.
- [80] Y. Lan, S. Farid, X. Meshik, K. Xu, M. Choi, S. Ranginwala, Y. Y. Wang, P. Burke, M. Dutta, M. A. Stroschio, *J. Sensors* **2018**, *2018*, 1.
- [81] R. S. Martin, R. A. Henningsen, A. Suen, S. Apparsundaram, B. Leung, Z. Jia, R. K. Kondru, M. E. Milla, *J. Pharmacol. Exp. Ther.* **2008**, *327*, 991.